Soft Matter

Nondestructive Characterization of Soft Materials and Biofilms by Measurement of Guided Elastic Wave Propagation Using Optical Coherence Elastography

Journal:	*Soft Matter*
Manuscript ID	SM-ART-09-2018-001902.R1
Article Type:	Paper
Date Submitted by the Author:	23-Nov-2018

Complete List of Authors:	Liou, Hong-Cin; Northwestern University, Mechanical Engineering Department Sabba, Fabrizio; Northwestern University, Civil and Environmental Engineering Department Packman, Aaron; Northwestern University, Civil and Environmental Engineering Department Wells, George; Northwestern University, Civil and Environmental Engineering Department Balogun, Oluwaseyi; Northwestern University, Mechanical Engineering Department; Northwestern University, Civil and Environmental Engineering Department

SCHOLARONE™
Manuscripts

Nondestructive Characterization of Soft Materials and Biofilms by Measurement of Guided Elastic Wave Propagation Using Optical Coherence Elastography

Hong-Cin Liou[1], Fabrizio Sabba[2], Aaron Packman[2], George Wells[2], Oluwaseyi Balogun[1,2]*

[1]Mechanical Engineering Department, Northwestern University, Evanston, IL 60208

[2]Civil and Environmental Engineering Department, Northwestern University, Evanston, IL 60208

[*]Corresponding author

o-balogun@u.northwestern.edu

+1-847-491-3054

ABSTRACT

Biofilms are soft multicomponent biological materials composed of microbial communities attached to surfaces. Despite the crucial relevance of biofilms to diverse industrial, medical, and environmental applications, biofilm mechanical properties are understudied. Moreover, most available techniques for characterization of biofilm mechanical properties are destructive. Here, we detail a model-based approach developed to characterize the viscoelastic properties of soft materials and bacterial biofilms based on experimental data obtained with the nondestructive dynamic optical coherence elastography (OCE) technique. The model predicted the frequency- and geometry-dependent propagation velocities of elastic waves in a soft viscoelastic plate supported by a rigid substratum. Our numerical calculations suggest that the dispersion curves of elastic waves recorded in thin soft plates by the dynamic OCE technique was dominated by guided waves, whose phase velocities strongly depended on the viscoelastic properties and the plate thicknesses. The numerical model was validated against experimental measurements in agarose phantom samples with different thicknesses and concentrations. The model was then used to interpret guided wave dispersion curves obtained by OCE technique in bacterial biofilms developed in a rotating annular reactor, which allowed for a quantitative characterization of biofilm shear modulus and viscosity. This study is the first to employ measurements of elastic wave propagation to characterize biofilms, and provides a novel framework combining a theoretical model and experimental approach for studying the relationship between biofilm internal physical structure and mechanical properties.

Keywords: nondestructive optoacoustic imaging, optical coherence elastography, viscoelastic properties, guided elastic wave propagation, biofilms

1. Introduction

Biofilms are multicomponent biological materials composed of communities of microorganisms attached to a surface and encased in a self-produced matrix of extracellular polymeric substances (EPS)[1, 2]. Biofilms are the dominant mode of microbial life in aquatic systems, soil and sediment, and play a critical role in biogeochemical cycling, food webs, and symbioses[3-6]. The mechanical properties of biofilms have recently attracted substantial attention from researchers but remain understudied[7-9]. It has been shown that biofilms display properties of both elastic solids and viscous liquids in response to stress, and can thus be viewed as viscoelastic biomaterials analogous to soft biological tissues[8, 10-12]. Biofilm mechanical properties depend on morphology and composition, and are thought to influence important processes like detachment, attachment, and mass transfer characteristics that are crucial to biofilm functions[13, 14]. Recent macro-scale quasi-static experiments on biofilm mechanical properties suggest that (1) biofilm mechanical properties are heterogeneous[8, 15]; (2) viscoelastic behavior occurs at small deformations[16, 17]; (3) viscoplastic behavior occurs at large deformations when the internal stresses are relieved[10, 15, 18, 19]; and (4) biofilms are stiffer near the attachment surface and more flexible in their canopy[20]. The latter suggests biofilm mechanical properties can vary with distance from the attachment surface.

Most work to date on biofilm mechanical properties has employed macro- and micro-rheological techniques to measure mechanical properties. These techniques have some limitations: macro-rheological techniques only measure bulk average of the properties and do not reveal spatial variability and complexity of living biofilms[21-23], whereas micro-rheological techniques yield only highly localized measurements, often on biofilms *ex situ*, and are not capable of spatial mapping at the mm to cm scale[24-28]. Additionally, these techniques require sample disruption or structural changes while testing. Recently, elastography techniques have enabled biomechanical characterization of soft structures, particularly in the biomedical engineering community, by combining diagnostic imaging tools with specimen deformation approaches. In these techniques, the spatial deformation of a biological specimen is mapped under an applied external force, allowing for identification of mechanical contrast regions and stiff tissues associated with different

disease states. Among existing elastography techniques including magnetic resonance elastography (MRE)[29], ultrasound elastography (USE)[30, 31], and optical coherence elastography (OCE)[32-34], the OCE technique provides superior characteristics such as (1) micron-scale spatial resolution, (2) high sample displacement sensitivity on the nanometer scale, and (3) high temporal resolution and fast image acquisition time. These features facilitate the detection of small sample deformations and provide the potential to track dynamic mechanical deformations in real time. OCE techniques can be classified as static or dynamic methods, depending on the time scale of the specimen deformation. Static OCE methods have been widely applied in biomechanical characterization experiments in the biomedical research community, where the heterogeneous strain map of tissue specimens produced in response to a uniform stress field is used to predict the local Young's modulus. This modulus is based on the ratio of the stress and strain, as obtained in a linear elastic solid. Measurements of viscoelastic properties, on the other hand, rely on tracking temporal dynamics of the specimen deformation under the applied stress field. This is achieved using dynamic OCE methods, in which creep relaxation dynamics[35], elastic stress wave propagation[36-41], or underdamped acoustic vibrations[42, 43] are recorded using various motion tracking methods. These methods can be classified into speckle tracking methods and phase sensitive optical coherence tomography (OCT). The latter is of great interest because it provides a larger measurement dynamic range and inexpensive options for data acquisition[38].

This paper provides the first-of-its-kind OCE characterization of viscoelastic properties in bacterial biofilms based on elastic stress wave propagation measurements. Elastic wave based dynamic OCE methods have been explored exclusively in biomedical applications for characterization of viscoelastic properties in soft tissues[36, 37, 44]; however, biofilms have more complex geometrical and compositional features. These features, including heterogeneous composition, surface roughness, non-uniform porosity distribution, and bacterial hierarchical stratification[11, 19, 45-47], make modeling of elastic waves in these materials challenging and invaluable for interpreting the experimental data. In this paper, we report a layered theoretical model that predicted the velocities of guided elastic waves at different frequencies in a soft viscoelastic plate with various thicknesses, shear moduli, and complex shear viscosities. The layered

model simulated a soft plate in contact with a semi-infinite water/vacuum medium and a rigid substratum, which approximates the sample geometries tested by the OCE technique. The theoretical model was validated against experimental measurements in agarose gel phantoms of different thicknesses and concentrations. Then, the model was applied to estimate the viscoelastic properties of a mixed-culture bacterial biofilm from OCE measurements of the dispersion curves at frequencies up to 1 kHz. This work provides a promising novel experimental framework for nondestructive quantification of biofilm viscoelastic properties based on elastic wave propagation measured by OCE technique. Furthermore, the potential to obtain co-registered 2D and 3D images of biofilm morphology and viscoelastic properties using the OCE technique can facilitate our understanding of the roles of composition, internal structure, and mechanical properties on the functional performance of bacterial biofilms in a range of applications of high societal relevance. Potential applications of the technique include characterizing fundamental biofilm properties in order to develop strategies to mitigate detrimental biofilms (biofouling) that lead to billions of dollars of cost per year in diverse water/wastewater, food, beverage, petrochemical, industrial equipment and piping, and medical settings[48, 49], and conversely to manage (retain) beneficial biofilms that are increasingly used to clean water and remediate groundwater and soil[50]. In addition, the application of OCE offers the opportunity to enhance understanding of material properties of biofilms in biofilm-linked infections that affect 17 million Americans annually, cause at least 550,000 deaths, and place an enormous economic burden on the US health care system[49].

2. Experimental section

2.1 Sample preparation

Soft agarose (Fisher Bioreagents, BP1423-500, PA, USA) gel phantoms with 1.0% and 2.0% weight-to-volume (w/v) concentrations were prepared by mixing one and two grams of agarose powder, respectively, with a 100 mL solution made from 94 mL of nano-purified water and 6 mL of 5.0% w/v skim milk (Becton, Dickinson and Company, 232100, MD, USA). Milk was used to enhance optical scattering in the agarose

samples and to improve the OCT image contrast of the sample morphology. A sample preparation protocol (Section S1 of the Supplemental Information) was followed to obtain samples with consistent mechanical properties and boundary flatness. A series of heterotrophic biofilm samples were also developed for method proof-of-concept using a rotating annular reactor (RAR Model 1320, Biosurface Technologies, Bozeman, MT, USA). The RAR was operated in batch mode for 24 hours after inoculation to allow for attachment of biomass to the coupons. After 24 hours, synthetic wastewater was fed into the RAR at a dilution rate of 5 d^{-1}. The system was inoculated with 25 mL of activated sludge from a local water reclamation plant (Hanover Park, IL, USA) and operated at 30 rpm and at a room temperature of 20-23°C. The reactor was constantly aerated and fed synthetic wastewater for 30 days in order to develop a thick mixed-culture bacterial biofilm, analogous to environmental biofilms commonly employed for contaminant removal in wastewater treatment biofilm reactors. The biofilm was predominantly composed of aerobic heterotrophs and growth was achieved on rectangular polycarbonate coupons designed with a special angled edge to match the slot inside the reactor and allowing them to stay in place during long duration experiments (width 12.7 mm, length 150 mm; Biosurface Technologies, Bozeman, MT, USA). Additional details of biofilm growth and reactor operation and monitoring are available in a recent publication from our research group[51]. After 30 days, and reaching a thickness of 2.5 mm, the coupon with intact biofilm was removed from the RAR and placed in the OCE setup to carry out measurements. Further details regarding OCE measurements of both agarose gel phantoms and biofilms are discussed in the next section.

2.2 Phase-sensitive optical coherence elastography

A schematic of the phase-sensitive OCE is shown in Fig. 1. The setup was used for local excitation and detection of elastic waves in the agarose gel phantoms and mixed-culture bacterial biofilm samples. In the setup, a paddle actuator, composed of a 10 mm wide razor blade glued to the end of an 18-gauge syringe needle, was used to excite elastic waves. The other end of the needle was attached to a piezoelectric transducer (Thorlabs PZS001) that was driven by a sinusoidal voltage from a radio frequency function generator (Agilent 33120A, CA, USA). The blade was guided towards the sample and made light contact

with the sample surface using a two-axis translation stage. When the piezoelectric transducer was excited, the blade indented the sample periodically and generated harmonic elastic waves including compressional waves, shear waves, and surface waves. Compressional and shear waves are bulk waves that travel into the sample, whereas surface waves travel near the sample boundary. A maximum 10 V of the peak-to-peak voltage applied to the transducer led to a peak-to-peak axial displacement of 5.8 μm of the needle. The local sample displacement induced by the elastic waves was then recorded with a phase-sensitive spectral-domain OCT system (operated with a near-infrared light source: center wavelength 930 nm and bandwidth 100 nm) that is capable of recording the sample morphology and the local dynamic response. The gray-scale sample morphology image was obtained by collecting a series of adjacent A-scans, which correspond to the one-dimensional scattering intensity along the vertical (z) direction through the depth of the sample, and assembling the A-scans to a two-dimensional B-scan image in the x-z plane. The intensity distribution in the B-scan image represents the spatial variation of the local refractive index in the sample, which is correlated with the sample's internal structure. In addition, the OCT acquired the local dynamic response in the sample by calculating the optical phase difference $\Delta\varphi$ between two adjacent A-scans recorded with a time delay dt, and relating $\Delta\varphi$ to the vertical component of the local sample displacement $u_z(x,z,t)$ by the relationship $\Delta\varphi(x,z,t) = {4\pi n(x,z)\Delta u_z(x,z,t)}/{\lambda_0}$, where n is the local refractive index of the sample and λ_0 is the center wavelength of the OCT light source. The motion of the scanning optics in the OCT system and the acquisition of the A-scans were synchronized with the sinusoidal driving function of the piezoelectric transducer using a custom-built microcontroller trigger circuit, so that the local phase difference $\Delta\varphi(x,z)$ along the x-direction could be recorded with respect to a fixed trigger reference and assembled together to obtain a 2D B-scan image. This image profiles the spatial distribution of the displacements induced by the waves. Additional details about the measurement approach of the dynamic response, especially the effect of the delay time *dt* on the measured data, are discussed in section S2 of the Supplemental Information.

Fig. 2 shows representative OCT and OCE B-scan images obtained in the 2.0% agarose gel phantom with 10 mm thickness. The sample was supported by a 1 mm thick glass substratum and loaded with a water layer over the top surface. The excitation frequency for this experiment was 1.4 kHz. The OCT and OCE images were acquired over a lateral distance of 9 mm. The sample was tilted by 10 degrees relative to the vertical optical axis of the microscope objective to eliminate strong direct reflection of the probe light from the air-water and the water-agarose interfaces that would create artifacts in the images due to multiple interferences. The bright band in the OCT image (Fig. 2a) is due to a strong contrast of the refractive index at the interface between the air and the water. In addition, the OCT image shows limited contrast in the agarose gel layer, suggesting the sample is homogeneous without apparent structural features such as voids or cracks. On the other hand, the OCE image (Fig. 2b) shows a periodic distribution of the phase difference $\Delta\varphi$ alternating between the maximum π and minimum $-\pi$ radians along the lateral direction which is associated with the periodic displacement of the elastic wave. The phase values were plotted within a smaller span $[-\pi/2,\pi/2]$ to enhance the color contrast. The spatial frequency ($\nu = 1/\lambda$, where λ is the wavelength) of the elastic wave was obtained by implementing spatial fast Fourier transform from the data along the white dotted line, and the phase velocity c of the elastic wave was determined based on the relationship $c = f\lambda$ where f is the excitation frequency. The measurement was repeated at different excitation frequencies to collect the frequency-dependent phase velocity, the dispersion curve, for the excited elastic waves in the sample. The dispersion curve of an agarose gel plate is a function of the plate thickness and material properties, which was used to determine the shear modulus and the shear viscosity through the inverse analysis based on the model presented in the following section.

2.3 Theoretical model for elastic wave propagation in a multi-layered structure

The choice of the elastic wave type used in measurements affects the achievable spatial resolution. In soft samples, the wavelength of compressional waves in the kHz range is typically in the range of meters, while the wavelength of shear waves in the same frequency range is three orders of magnitude smaller. As such, shear waves in the kHz range are favored for acoustic mapping of elastic property variations in soft

samples[52]. Operating with shear waves at MHz frequencies can lead to spatial resolution in the micron and sub-micron range; however, this is prohibited by attenuation of elastic waves resulting from the viscoelastic behavior of the materials. Furthermore, in thin samples where the elastic wavelength is comparable to the sample thickness, shear waves reflect from the sample boundaries and overlap through the sample thickness to produce standing wave interference patterns and propagate as guided waves in the lateral direction[53-55]. These guided waves can propagate as Lamb, Love, or surface acoustic waves, having dispersive phase velocities that depend on frequency, sample geometry, and sample material properties. Therefore, a model capable of predicting the dispersion curves of the guided waves is necessary for the inverse analysis which estimates the viscoelastic properties in the samples from the experimental measurements of wave velocity.

In this section, we present a model for guided elastic wave propagation in a multi-layer structure composed of an isotropic, viscoelastic, and homogenous gel plate loaded by a water half-space on the top surface and attached to a stiff half-space at the bottom surface. A schematic diagram of the layered model system is shown in Fig. 3. The stiff (glass) substrate was assumed to be rigid since its Young's and shear moduli are orders of magnitude larger than those of the agarose gel layer. The water layer was assumed to be an ideal liquid which is homogenous, isotropic, inviscid, and does not support shear stresses. The model predicts the dispersion relation for the water loaded viscoelastic layer based on the solution to the elastodynamic wave equation for an isotropic and homogeneous material in the frequency domain, given by[56]

$$(\lambda^* + \mu^*)\nabla(\nabla \cdot \vec{u}) + \mu^* \nabla^2 \vec{u} + \rho\omega^2 \vec{u} = 0 \quad (1)$$

where $\vec{u} = u_x \hat{e}_x + u_y \hat{e}_y + u_z \hat{e}_z$ is the displacement vector which comprises its components u_x, u_y, and u_z along x-, y-, and z- Cartesian axes with unit vectors $\hat{e}_x$, $\hat{e}_y$, and $\hat{e}_z$. ∇ is the differential operator in the three-dimensional space, ω is the angular frequency, ρ is the material density, and λ^* and μ^* are the complex frequency-dependent relaxation functions of the Lamé material properties defined by

$$\lambda^*(\omega) = \lambda + i\eta_\lambda \omega \quad (2)$$

$$\mu^*(\omega) = \mu + i\eta_\mu \omega \quad (3)$$

where λ and μ are the asymptotic values of the relaxation functions, and η_λ and η_μ are complex viscosity terms. μ and η_μ represent the shear modulus and shear viscosity[57, 58], respectively, which are of particular interest in this work. It can be shown that the solution to eqn (1) under plane strain conditions ($u_y = 0, \partial/\partial y = 0$) in a plate is a linear superposition of compressional and shear waves, which can be expressed in terms of a scalar potential ϕ and vector potential component ψ given by

$$\phi = A_{L+} e^{i(k_x x + k_z^L z - \omega t)} + A_{L-} e^{i(k_x x - k_z^L z - \omega t)} \tag{4}$$

$$\psi = A_{S+} e^{i(k_x x + k_z^S z - \omega t)} + A_{S-} e^{i(k_x x - k_z^S z - \omega t)} \tag{5}$$

where $A_{L\pm}$ and $A_{S\pm}$ are complex amplitude constants with the letters L and S distinguishing partial longitudinal and shear waves and the $\pm$ sign distinguishing downward (positive) and upward (negative) traveling directions of the partial bulk waves as illustrated in Fig. 3. $k_z^{L,S}$ are the complex wave numbers in the vertical (z) direction which satisfy the following relationship:

$$\pm k_z^L = \pm \sqrt{\frac{\omega^2}{a_L^2} - k_x^2} \tag{6}$$

$$\pm k_z^S = \pm \sqrt{\frac{\omega^2}{a_S^2} - k_x^2} \tag{7}$$

where a_L and a_S are complex compressional and shear wave speeds, which are related to the material properties by the following relationships:

$$a_L^2 = \frac{\lambda^* + 2\mu^*}{\rho} \tag{8}$$

$$a_S^2 = \frac{\mu^*}{\rho} \tag{9}$$

The real parts of a_L and a_S yield the bulk compressional and shear wave speeds, c_L and c_S, and their imaginary values are the attenuation coefficients of the bulk waves. The local displacement vector associated with the harmonic plane wave potential solutions is obtained using the vector relationship:

$$\vec{\boldsymbol{u}} = \nabla\phi + \nabla \times \vec{\boldsymbol{\psi}} \tag{10}$$

where $\vec{\boldsymbol{u}} = (u_x,0,u_z)$ and $\vec{\boldsymbol{\psi}} = (0,\psi,0)$ under plane strain conditions. The local stress tensor is given by the Lamé constitutive relations

$$\sigma_{zz} = \lambda^* (\varepsilon_{xx} + \varepsilon_{zz}) + 2\mu^* \varepsilon_{zz} \tag{11}$$

$$\sigma_{xz} = 2\mu^* \varepsilon_{xz} \tag{12}$$

where $\varepsilon_{xx} = \frac{\partial u_x}{\partial x}$, $\varepsilon_{zz} = \frac{\partial u_z}{\partial z}$, and $\varepsilon_{xz} = \frac{1}{2}\left(\frac{\partial u_x}{\partial z} + \frac{\partial u_z}{\partial x}\right)$ [57, 59-61].

From eqn (4) to (12), the components of the local displacement and stress tensor are expressed in the matrix form:

$$\begin{bmatrix} u_x \\ u_z \\ \sigma_{zz} \\ \sigma_{xz} \end{bmatrix} = i\boldsymbol{D} \begin{bmatrix} A_{L+} \\ A_{L-} \\ A_{S+} \\ A_{S-} \end{bmatrix} \exp\left[i\left(k_x x - \omega t\right)\right]$$

where

$$\boldsymbol{D} = \begin{bmatrix} k_x e^{ik_z^L z} & k_x e^{-ik_z^L z} & -k_z^S e^{ik_z^S z} & k_z^S e^{-ik_z^S z} \\ k_z^L e^{ik_z^L z} & -k_z^L e^{-ik_z^L z} & k_x e^{ik_z^S z} & k_x e^{-ik_z^S z} \\ i\rho(\omega^2 - 2\alpha_S^2 k_x^2) e^{ik_z^L z} & i\rho(\omega^2 - 2\alpha_S^2 k_x^2) e^{-ik_z^L z} & 2i\rho k_x k_z^S \alpha_S^2 e^{ik_z^S z} & -2i\rho k_x k_z^S \alpha_S^2 e^{-ik_z^S z} \\ 2i\rho k_x k_z^L \alpha_S^2 e^{ik_z^L z} & -2i\rho k_x k_z^L \alpha_S^2 e^{-ik_z^L z} & -i\rho(\omega^2 - 2\alpha_S^2 k_x^2) e^{ik_z^S z} & -i\rho(\omega^2 - 2\alpha_S^2 k_x^2) e^{-ik_z^S z} \end{bmatrix} \tag{13}$$

The local displacement vector in the water layer can be expressed in terms of a potential function ϕ^w by the relationship:

$$\overrightarrow{\boldsymbol{u^w}} = \nabla\phi^w, \tag{14}$$

which is a special case of eqn (10) where the vector potential ψ, related to the shear partial waves, vanishes. The scalar potential in eqn (14) must satisfy the wave equation

$$\nabla^2\phi^w + \left(k^w\right)^2\phi^w = 0 \tag{15}$$

where $(k^w)^2 = k_x^2 + (k_z^w)^2$ is the wavenumber of the compressional wave in the water layer that comprises the components k_x and k_z^w in x- and z-directions and has the relation with the compressional wave speed $k^w = \omega/c^w$ as $c^w =$ 1481 m/s in water. The water layer is treated as a half-space without wave sources. As such, only partial waves travelling in the negative z-direction exist, as illustrated in Fig. 3. In addition, we seek guided elastic wave solutions in the soft plate that travel at the water-plate interface as interface waves[62-64], so the scalar potential can be expressed with the amplitude $A_{L}^{w}{}_{-}$ and the wavenumber k_x by

$$\phi^w = \left(A_{L}^{w}{}_{-}\, e^{-ik_z^w z}\right)\exp\left[i\,(k_x x - \omega t)\right] \tag{16}$$

From eqn (11), (12), (14) and (16), the displacement and the pressure (equivalent to the normal stresses in solids) in the vertical direction in the water layer, u_z^w and p, can be derived

$$u_z^w = -i\left(k_z^w e^{-ik_z^w z}\right)A_{L}^{w}{}_{-}\exp\left[i(k_x x - \omega t)\right] \tag{17}$$

$$p = i(i\rho^w\omega^2 e^{-ik_z^w z})A_{L}^{w}{}_{-}\exp\left[i(k_x x - \omega t)\right] \tag{18}$$

Since the water layer was assumed to be an inviscid liquid that does not support the propagation of shear waves, the shear stress in the water layer is zero, $\sigma_{xz}^w = 0$.

Five boundary conditions are needed to solve for the unknown coefficients for the potential functions in the soft plate and water layers. The boundary conditions include zero displacement at the bottom surface of the soft plate, $u_x|_{z=h} = u_z|_{z=h} = 0$, due to the rigid glass substratum, continuity of the vertical displacements between the soft plate and the water layer, $u_z|_{z=0} = u_z^w|_{z=0}$, continuity of the normal traction in the soft plate and the pressure in the water, $\sigma_{zz}|_{z=0} = p|_{z=0}$, and zero shear traction at the interface between the soft plate and the water layer, $\sigma_{xz}|_{z=0} = 0$. Applying these conditions leads to five equations for the potential function coefficients, which are expressed below in the matrix form

$$\begin{bmatrix} k_x e^{ik_z^L h} & k_x e^{-ik_z^L h} & -k_z^S e^{ik_z^S h} & k_z^S e^{-ik_z^S h} & 0 \\ k_z^L e^{ik_z^L h} & -k_z^L e^{-ik_z^L h} & k_x e^{ik_z^S h} & k_x e^{-ik_z^S h} & 0 \\ i\rho(\omega^2 - 2\alpha_S^2 k_x^2) & i\rho(\omega^2 - 2\alpha_S^2 k_x^2) & 2i\rho k_x k_z^S \alpha_S^2 & -2i\rho k_x k_z^S \alpha_S^2 & -i\rho^w \omega^2 \\ 2i\rho k_x k_z^L \alpha_S^2 & -2i\rho k_x k_z^L \alpha_S^2 & -i\rho(\omega^2 - 2\alpha_S^2 k_x^2) & -i\rho(\omega^2 - 2\alpha_S^2 k_x^2) & 0 \\ k_z^L & -k_z^L & k_x & k_x & k_z^w \end{bmatrix} \begin{bmatrix} A_{L+} \\ A_{L-} \\ A_{S+} \\ A_{S-} \\ A_{L-}^w \end{bmatrix} = \mathbf{0} \quad (18)$$

or

$$\boldsymbol{SA} = \mathbf{0} \quad (19)$$

To obtain non-trivial solutions for $\boldsymbol{A}$ from eqn (19), the determinant of the coefficient matrix $\boldsymbol{S}$ must equal to zero:

$$\det(\boldsymbol{S}) = 0 \quad (20)$$

which is the characteristic equation of the layered model. The solutions (ω,k_x) of eqn (20) yield the dispersion relation of the guided elastic waves in the water-loaded viscoelastic layer as the speed of the elastic wave propagating along the *x*-direction, $c = \omega/k_x$.

3. Results and discussion

3.1. Numerical simulation

In this section, we present a set of dispersion curves predicted by the model for the guided elastic waves in the layered structure under different boundary conditions and mechanical properties as shown in Fig. 4. Each dispersion curve represents a unique elastic wave mode associated with a group of the solutions (ω, k_x) of eqn (20). Although there are an infinite number of dispersion curves for the model since the frequency can go to infinity, we only plotted the curves within the frequency range 0-3000 Hz. First, we calculated the dispersion curves for a purely elastic plate with the mechanical properties and geometry such as compressional wave speed $c_L =$ 1481 m/s, shear wave speed $c_S =$ 3 m/s, zero complex viscosities $\eta_\lambda = \eta_\mu = 0$, and layer thickness h = 10 mm. The compressional wave speed in the gel was assumed to be the same

as found in water because of the low concentration of agar in the gel phantoms. The large ratio of the compressional to the shear wave speeds corresponds to a Poisson's ratio of 0.5.

Fig. 4a shows the results from the stress-free and clamped boundary conditions imposed on the top and the bottom surfaces of the agarose layer, in which the water layer in Fig. 3 was replaced by vacuum. Except for the non-dispersive mode with a frequency-independent phase velocity c_S, corresponding to the bulk shear wave propagation, each dispersion curve has a cut-off frequency (f_c) below which the associated elastic wave mode does not propagate. The cut-off frequencies occur at values of $f_c = \frac{c_S}{2h}, \frac{c_S}{h}, \frac{3c_S}{2h}, \frac{2c_S}{h}$ [58], etc. where the phase velocity tends to approach infinity. An implication of the infinite phase velocity at the cut-off frequency is that all points on the free surface of the layer vibrates in phase, leading to a shear-thickness resonance. We note that the phase velocities of all dispersive modes have decreasing trends with frequency and asymptotically approach the bulk shear wave speed c_S, except for the first mode. The asymptotic value of the first mode is the Rayleigh wave velocity of the layer, c_R = 2.87 m/s. The ratio $c_R/c_S =$ 0.96 agrees with the theoretical prediction for a material that has a Poisson's ratio of 0.5[62, 63]. The penetration depth of the Rayleigh wave is approximately one wavelength, over which the energy of the wave attenuates to 1/*e* of its maximum value at the layer surface. As such, the elastic mode reaches the asymptotic value and propagates as a pure surface wave without the interference by the energy reflected from the bottom surface. As an example, consider an agarose gel phantom with thickness 10 mm. When the frequency is larger than 500 Hz, the wavelength is 5.7 mm, which is smaller than the thickness of the agarose gel layer.

When the agarose gel layer is loaded with water on the top surface, the water loading decreases the Rayleigh wave velocity to the Scholte wave velocity $c_{Sch} =$ 2.52 m/s as shown in Fig. 4b. The Scholte wave propagates at the interface between the gel and the water layers whose elastic energy is attenuated along the transverse direction as part of the energy couples into the water layer. The ratio $c_{Sch}/c_S =$ 0.84 from our numerical calculation agrees well with analytical predictions[62, 63].

Fig. 4c shows the dispersion curves predicted by the model for a water-loaded viscoelastic layer of agarose gel. In this calculation, the material properties and the plate geometry remained the same as the

ones used to obtain the results shown in Fig. 4a and 4b, with the sole exception that the complex shear viscosity was changed to η_μ = 0.15 Pa-s. One significant difference between the dispersion curves in Fig. 4b and 4c is the increasing bulk shear and Scholte wave velocities in the high-frequency region due to the effect of viscosity, which is of particularly interest in this study. Measurement of the dispersive phase velocity over this region can support characterization of the shear modulus and complex shear viscosity of the agarose gel sample. The dispersion curves also depend on the layer thickness as shown in Fig. 5, where the layer thickness is changed to 1 mm with the same material properties as in Fig. 4c. Comparing Fig. 5 with Fig. 4c, the most significant difference is that only three elastic modes are supported in the 1 mm thick layer, which correspond to the lowest interface wave, the bulk shear wave, and the second guided wave modes. The lowest mode in Fig. 5 has a higher cut-off frequency since this frequency is inversely proportional to the layer thickness.

3.2. Experimental results

3.2.1. Agarose gel phantoms

Fig. 6 shows experimental dispersion curves obtained for the 1.0% and 2.0% agarose gel phantoms of two thicknesses, 10 mm and 1 mm. The bandwidth of the measured dispersion curves was limited to 5 kHz due to the low signal-to-noise ratio of the OCE B-scans, which stemmed from attenuation of the excited waves above this frequency. Each dispersion curve in Fig. 6 represents the average of nine measurements of the phase velocity versus frequency obtained at random positions in the sample. The error bars represent the standard deviation of these nine measurements. For all the experimental dispersion curves, the coefficient of variation (COV), defined as the ratio of standard deviation to the average value of the phase velocity, is less than 2.5%, suggesting homogeneity of the sample elastic properties. The dispersion curves for the 1 mm thick samples have a relatively constant wave speed within the high frequency range. The wavelength of the excited waves in the 1.0% agarose sample, for example, decreased from 1.29 mm to 0.38 mm between the frequency range of 1.2 to 4 kHz, which suggests that the excited wave changed from a guided wave at

lower frequencies to a Scholte wave at higher frequencies. On the other hand, for the 10 mm thick samples, the Scholte wave mode was supported over the frequency bandwidth of the measurement since the wavelength was smaller than the sample thickness. As observed in the numerically-calculated dispersion curves, the phase velocity of the wave modes obtained in the 10 mm samples increase markedly with frequency due to the complex shear viscosity of the samples. In addition, the average phase velocity increased with the agarose concentration in the gel, as expected.

The dispersion curves in Fig. 6b have a decreasing trend in the low-frequency range, indicating that the measured mode belongs to the lowest elastic mode illustrated in Fig. 4. This is a reasonable observation since the Scholte wave was the predominant propagation mode near the interface[63, 65]. Fig. 7 compares numerical calculations of the dispersion curve for the first mode in the layered model to the experimental data. The shear modulus and complex shear viscosity were used as free fitting parameters in the numerical model for samples of 10 mm thickness, while shear modulus was the only free fitting parameter for samples of 1 mm thickness owing to the limited dispersion observed in these experiments. Good agreement was found between the experimental and numerical results, except for the larger errors observed within the low frequency range in Fig. 7c and 7d, which were due to lack of sufficient periodic cycles of the waves within the OCE field of view to estimate the wavelength through fast Fourier transform. The shortest wavelength below 2 kHz in Fig. 7c and 7d was 1.65 mm; this is equivalent to less than six cycles within the total sampling distance in the OCE B-scan, which limited the accuracy of the wavelength estimation. The best-fit material properties for the samples are listed in Table 1. The shear modulus and viscosity increase, as expected, with the concentration of agarose in the gel. The shear moduli measured from 1 and 10 mm samples were similar at 1.0% and indistinguishable at 2.0%, and the values agree well with those reported in the literature[38, 52]. This finding validates the use of the layered model to determine the mechanical properties of viscoelastic materials.

3.2.2. Mixed-culture bacterial biofilm

After 30 days of growth, the mixed-culture bacterial biofilm reached a ~2.5 mm thickness with a ~ 250 μm variation over a 4 mm lateral extent due to surface roughness as shown in the OCT B-scan (Fig. 8a) that illustrates the sample morphology. The OCE B-scan obtained at an excitation frequency of 660 Hz and the dispersion curves from the numerical simulation and experimental measurements are shown in Fig. 8b and 8c, respectively. In order to more precisely calculate the speed of the elastic wave travelling along the curved surface, a cubic function was fitted to the curved region of the biofilm surface to approximate the propagation path of the elastic waves. The amplitudes at discrete intervals along the path were extracted, and the fast Fourier transform was applied to the data to obtain the spatial frequency (or inverse wavelength) of the elastic waves (See Section S4 in the Supplemental Information). The maximal excitation frequency in the measurement was limited to 1 kHz due to attenuation of elastic waves in the sample. Unlike the agarose gel sample, the OCT image of the biofilm shows internal structural variations due to the presence of pores (dark bands), which also results in the low phase amplitude of the elastic waves in the OCE image. This finding aligns with other observations that pores and structural heterogeneity are common in biofilms[13, 66].

The bright white bands in the OCT image (Fig. 8a) indicate the boundary of the biofilm with air, and the propagation mode illustrated in the OCE image (Fig. 8b) is a Rayleigh surface wave. The use of the Rayleigh wave measurement is particularly advantageous in this case since the penetration depths of the wave, 1.2 mm at 550 Hz and 0.76 mm at 1 kHz, were less than the sample thickness and thus less sensitive to sample thickness variations. The dispersion curve for the measured data in Fig. 8c shows a 15% increase in phase velocity within the frequency bandwidth of the measurement. The measured dispersion curve was fitted by the numerical model using the biofilm shear modulus and viscosity as free fitting parameters. Similar to Fig. 7c and 7d, large disagreement between the experimental data and the numerical model is observed within the low frequency range (≤ 400 Hz) due to the limited number of wavelengths within the total sampling distance. The best-fit shear modulus and complex shear viscosity are 429 Pa and 0.06 Pa-s. These estimated properties represent the average bulk viscoelastic properties of the biofilm, and are within the broad range of reported values for the viscoelastic properties of biofilms (shear modulus = 10^{-1} - 10^{5} Pa

and viscosity = 10^{-1} - 10^{10} Pa-s)[18]. The broad range reflects both the diversity of different type of biofilms used in other studies and additional differences resulting from the inconsistencies and disadvantages of the characterization methods used. We highlight that most of the rheometry techniques employed for property characterization are destructive or involve large disturbances in sample geometry when testing, which inevitably causes changes of the sample morphology and properties. On contrary, our novel technique has a nondestructive nature that prevents any structural change and allows for the estimation of viscoelastic properties in the intact forms of the samples, which makes this more advantageous compared to other techniques.

We remark that in our inverse modeling analysis, we assumed the bulk modulus of the biofilm to be equal to the bulk modulus of water due to high water content (> 90%) of the sample. Overall, this novel approach provides a nondestructive, direct, local and *in situ* option to interrogate mechanical properties in these type of systems. Further work that refines the layered model is needed to address the heterogeneous spatial distribution of the shear modulus in the sample as suggested in Fig. 8b.

4. Conclusion

We developed methods involving a combination of OCE measurements and inverse modeling to characterize the mechanical properties of soft viscoelastic materials and bacterial biofilms. OCE was employed to obtain the dispersion curve—the frequency-dependent phase velocity—of the surface acoustic wave travelling in a biofilm supported by a rigid substrate. This is the first work to present wave propagation in biofilms, discover the frequency-dependent wave velocity, and interpret the dispersive wave velocity by a theoretical model to estimate the mechanical properties. The theoretical model obtained the dispersion curves of guided elastic wave modes by solving the elastodynamic wave equation for a layered viscoelastic plate attached to a rigid substratum and a semi-infinite water/vacuum layer on both sides. Dispersion in these materials depends on the mechanical properties, the geometry of the plate, and the presence or absence of water on the surface of the viscoelastic material. The model was validated by estimating the shear moduli

and complex shear viscosities from the OCE measurements of phase velocities in 10 and 1 mm thick agarose gel plates with 1.0% and 2.0% agarose concentrations. The estimation of the agarose gel properties agrees well with the ones in literature. These results suggest that the wave propagation observed in the OCE measurements of agarose gel plates belong to the lowest elastic mode travelling near the top boundary of the plate. The influence of the plate geometry is crucial since the guided waves interact with the bottom boundary when the acoustic wavelength is larger than the plate thickness. We then used this approach to measure the shear modulus and complex shear viscosity in a bacterial biofilm, and obtained reasonable results that are within the range reported in literature. Since there is no "gold standard" measurement for mechanical properties in soft materials and biofilms, our nondestructive technique provides a novel approach for characterizing these properties without affecting the original status of the samples. Furthermore, this framework enhances our understanding of elastic wave propagation in soft viscoelastic materials and provides a first proof-of-concept of OCE application to quantify mechanical properties of biofilms that are critically important in diverse environments and applications. The OCE technique can be further employed to study relationships between biofilm morphology, growth conditions, and elastic properties. Future work should focus on refining the layered model to address variations of the geometry and heterogeneity of material properties in soft materials as well as on utilizing the technique for rapid, nondestructive, spatially-resolved characterization of biofilm mechanical properties across a range of microbial systems and applications.

Conflicts of interest

The authors declare no conflicts of interest.

Acknowledgements

The authors thank Dr. Claire Prada (Institute Langevin, France) for the useful discussion regarding the development of the multi-layered model and Dr. Alex Rosenthal (inCTRL, Canada) for his insights on biofilms and rotating annular reactor operation. The authors also acknowledge the support of the National

Science Foundation via Award CBET-1701105, and the Civil and Environmental Engineering Department at Northwestern University for providing seed funding for this project.

REFERENCES

1. L. Hall-Stoodley, J. W. Costerton and P. Stoodley, *Nat Rev Micro*, 2004, **2**, 95-108.
2. J. N. Wilking, T. E. Angelini, A. Seminara, M. P. Brenner and D. A. Weitz, *MRS Bulletin*, 2011, **36**, 385-391.
3. H.-C. Flemming, J. Wingender, U. Szewzyk, P. Steinberg, S. A. Rice and S. Kjelleberg, *Nat. Rev. Micro.*, 2016, **14**, 563-575.
4. J. W. Costerton, Z. B. Lewandowski, D. E. Caldwell, D. R. Korber and H. M. Lappin-Scott, *Annu Rev Microbiol*, 1995, **49**, 711-745.
5. T. J. Battin, W. T. Sloan, S. Kjelleberg, H. Daims, I. M. Head, T. P. Curtis and L. Eberl, *Nat Rev Micro*, 2007, **5**, 76-81.
6. T. J. Battin, K. Besemer, M. M. Bengtsson, A. M. Romani and A. I. Packmann, *Nat. Rev. Micro.*, 2016, **14**, 251-263.
7. B. Halan, K. Buehler and A. Schmid, *Trends Biotechnol*, 2012, **30**, 453-465.
8. N. Billings, A. Birjiniuk, T. S. Samad, P. S. Doyle and K. Ribbeck, *Rep Prog Phys*, 2015, **78**, 036601.
9. H. C. Flemming, J. Wingender and U. Szewzyk, *Biofilm Highlights*, Springer Berlin Heidelberg, 2011.
10. I. Klapper, C. J. Rupp, R. Cargo, B. Purvedorj and P. Stoodley, *Biotechnol Bioeng*, 2002, **80**, 289-296.
11. J. N. Wilking, T. E. Angelini, A. Seminara, M. P. Brenner and D. A. Weitz, *MRS Bulletin*, 2011, **36**, 385-391.
12. S. Bhat, D. Jun, B. C and T. E. S Dahms, in *Viscoelasticity - From Theory to Biological Applications*, 2012, DOI: 10.5772/49980, ch. Chapter 6.
13. H. Boudarel, J. D. Mathias, B. Blaysat and M. Grediac, *NPJ Biofilms Microbiomes*, 2018, **4**, 17.
14. Y. He, B. W. Peterson, M. A. Jongsma, Y. Ren, P. K. Sharma, H. J. Busscher and H. C. van der Mei, *PLoS One*, 2013, **8**, e63750.
15. M. Bol, A. E. Ehret, A. Bolea Albero, J. Hellriegel and R. Krull, *Crit Rev Biotechnol*, 2013, **33**, 145-171.
16. N. Aravas and C. S. Laspidou, *Biotechnol Bioeng*, 2008, **101**, 196-200.
17. A. K. Ohashi, T.; Syutsubo, K.; Harada, H., *Water Sci. & Technol.*, 1999, **39**, 261-268.
18. B. W. Peterson, Y. He, Y. Ren, A. Zerdoum, M. R. Libera, P. K. Sharma, A. J. van Winkelhoff, D. Neut, P. Stoodley, H. C. van der Mei and H. J. Busscher, *FEMS Microbiol Rev*, 2015, **39**, 234-245.
19. P. Stoodley, K. Sauer, D. G. Davies and J. W. Costerton, *Annu Rev Microbiol*, 2002, **56**, 187-209.
20. E. C. Hollenbeck, C. Douarche, J. M. Allain, P. Roger, C. Regeard, L. Cegelski, G. G. Fuller and E. Raspaud, *J Phys Chem B*, 2016, **120**, 6080-6088.
21. O. Galy, P. Latour-Lambert, K. Zrelli, J. M. Ghigo, C. Beloin and N. Henry, *Biophys J*, 2012, **103**, 1400-1408.
22. V. Korstgens, H. C. Flemming, J. Wingender and W. Borchard, *J Microbiol Methods*, 2001, **46**, 9-17.
23. B. W. Towler, C. J. Rupp, A. B. Cunningham and P. Stoodley, *Biofouling*, 2003, **19**, 279-285.
24. S. Aggarwal, E. H. Poppele and R. M. Hozalski, *Biotechnol Bioeng*, 2010, **105**, 924-934.

25. D. N. Hohne, J. G. Younger and M. J. Solomon, *Langmuir*, 2009, **25**, 7743-7751.
26. J. D. Mathias and P. Stoodley, *Biofouling*, 2009, **25**, 695-703.
27. P. C. Lau, J. R. Dutcher, T. J. Beveridge and J. S. Lam, *Biophys J*, 2009, **96**, 2935-2948.
28. F. C. Cheong, S. Duarte, S.-H. Lee and D. G. Grier, *Rheologica Acta*, 2008, **48**, 109-115.
29. A. Manduca, T. E. Oliphant, M. A. Dresner, J. L. Mahowald, S. A. Kruse, E. Amromin, J. P. Felmlee, J. F. Greenleaf and R. L. Ehman, *Med Image Anal*, 2001, **5**, 237-254.
30. T. A. Krouskop, T. M. Wheeler, F. Kallel, B. S. Garra and T. Hall, *Ultrasonic imaging*, 1998, **20**, 260-274.
31. J. Ophir, I. Cespedes, H. Ponnekanti, Y. Yazdi and X. Li, *Ultrasonic imaging*, 1991, **13**, 111-134.
32. B. F. Kennedy, K. M. Kennedy and D. D. Sampson, *IEEE Journal of Selected Topics in Quantum Electronics*, 2014, **20**, 272-288.
33. X. Liang, V. Crecea and S. A. Boppart, *J Innov Opt Health Sci*, 2010, **3**, 221-233.
34. M. Wagner and H. Horn, *Biotechnol Bioeng*, 2017, **114**, 1386-1402.
35. X. Liang, S. G. Adie, R. John and S. A. Boppart, *Opt Express*, 2010, **18**, 14183-14190.
36. L. Ambrozinski, S. Song, S. J. Yoon, I. Pelivanov, D. Li, L. Gao, T. T. Shen, R. K. Wang and M. O'Donnell, *Sci Rep*, 2016, **6**, 38967.
37. M. Razani, T. W. Luk, A. Mariampillai, P. Siegler, T. R. Kiehl, M. C. Kolios and V. X. Yang, *Biomed Opt Express*, 2014, **5**, 895-906.
38. S. Song, Z. Huang, T. M. Nguyen, E. Y. Wong, B. Arnal, M. O'Donnell and R. K. Wang, *J Biomed Opt*, 2013, **18**, 121509.
39. S. Song, N. M. Le, Z. Huang, T. Shen and R. K. Wang, *Opt Lett*, 2015, **40**, 5007-5010.
40. Q. Wang, G. Jiang, L. Ye, M. Pijuan and Z. Yuan, *Water Res*, 2014, **62**, 202-210.
41. J. Zhu, Y. Qu, T. Ma, R. Li, Y. Du, S. Huang, K. K. Shung, Q. Zhou and Z. Chen, *Opt Lett*, 2015, **40**, 2099-2102.
42. V. Crecea, A. L. Oldenburg, X. Liang, T. S. Ralston and S. A. Boppart, *Opt Express*, 2009, **17**, 23114-23122.
43. P. C. Huang, P. Pande, A. Ahmad, M. Marjanovic, D. R. Spillman, Jr., B. Odintsov and S. A. Boppart, *IEEE J Sel Top Quantum Electron*, 2016, **22**.
44. S. Wang, A. L. Lopez, 3rd, Y. Morikawa, G. Tao, J. Li, I. V. Larina, J. F. Martin and K. V. Larin, *Biomed Opt Express*, 2014, **5**, 1980-1992.
45. R. M. Donlan, *Emerg Infect Dis*, 2002, **8**, 881-890.
46. J. Wimpenny, W. Manz and U. Szewzyk, *FEMS Microbiol Rev*, 2000, **24**, 661-671.
47. J. W. Costerton, Z. Lewandowski, D. E. Caldwell, D. R. Korber and H. M. Lappin-Scott, *Annu Rev Microbiol*, 1995, **49**, 711-745.
48. H.-C. Flemming, in *Biofilm Highlights*, eds. H.-C. Flemming, J. Wingender and U. Szewzyk, Springer Berlin Heidelberg, Berlin, Heidelberg, 2011, DOI: 10.1007/978-3-642-19940-0_5, pp. 81-109.
49. V. D. Gordon, M. Davis-Fields, K. Kovach and C. A. Rodesney, *Journal of Physics D: Applied Physics*, 2017, **50**, 223002.
50. WEF, *WEF Manual of Practice 35: Biofilm Reactors*, WEF Press, Alexandria, VA, 2011.
51. A. F. Rosenthal, J. S. Griffin, M. Wagner, A. I. Packman, O. Balogun and G. F. Wells, *Biotechnol Bioeng*, 2018, **115**, 2268-2279.
52. M. Couade, M. Pernot, C. Prada, E. Messas, J. Emmerich, P. Bruneval, A. Criton, M. Fink and M. Tanter, *Ultrasound Med Biol*, 2010, **36**, 1662-1676.
53. J. Laperre and W. Thys, *The Journal of the Acoustical Society of America*, 1993, **94**, 268-278.
54. Z. Zhu and J. Wu, *The Journal of the Acoustical Society of America*, 1995, **98**, 1057-1064.
55. F. Simonetti, *The Journal of the Acoustical Society of America*, 2004, **115**, 2041-2053.
56. J. D. Achenbach, in *Wave Propagation in Elastic Solids*, ed. J. D. Achenbach, Elsevier, Amsterdam, 1975, DOI: 10.1016/b978-0-7204-0325-1.50008-4, pp. 79-121.
57. M. J. S. Lowe, *IEEE Transactions on Ultrasonics, Ferroelectrics and Frequency Control*, 1995, **42**, 525-542.

58. J. L. Rose, *Ultrasonic Waves in Solid Media*, Cambridge University Press, 1999.
59. N. A. Haskell, *Bulletin of the Seismological Society of America*, 1953, **43**, 17-34.
60. B. Pavlakovic, M. Lowe, D. Alleyne and P. Cawley, in *Review of Progress in Quantitative Nondestructive Evaluation*, eds. D. O. Thompson and D. E. Chimenti, Springer US, Boston, MA, 1997, DOI: 10.1007/978-1-4615-5947-4_24, ch. Chapter 24, pp. 185-192.
61. W. T. Thomson, *Journal of Applied Physics*, 1950, **21**, 89-93.
62. M. A. Kirby, I. Pelivanov, S. Song, L. Ambrozinski, S. J. Yoon, L. Gao, D. Li, T. T. Shen, R. K. Wang and M. O'Donnell, *J Biomed Opt*, 2017, **22**, 1-28.
63. I. A. Viktorov, *Rayleigh and Lamb Waves*, Springer US, 1 edn., 1967.
64. J. Zhu, J. S. Popovics and F. Schubert, *The Journal of the Acoustical Society of America*, 2004, **116**, 2101-2110.
65. C. B. Scruby and L. E. Drain, *Laser Ultrasonics Techniques and Applications*, Taylor & Francis, 1990.
66. M. Jafari, P. Desmond, M. C. M. van Loosdrecht, N. Derlon, E. Morgenroth and C. Picioreanu, *Water Res*, 2018, **145**, 375-387.

Figures

Nondestructive Characterization of Soft Materials and Biofilms by Measurement of Guided Elastic Wave Propagation Using Optical Coherence Elastography

Hong-Cin Liou[1], Fabrizio Sabba[2], Aaron Packman[2], George Wells[2], Oluwaseyi Balogun[1,2]*

[1]Mechanical Engineering Department, Northwestern University, Evanston, IL 60208

[2]Civil and Environmental Engineering Department, Northwestern University, Evanston, IL 60208

***Corresponding author:**

Oluwaseyi Balogun, Phone: +1 847-491-3054; e-mail: o-balogun@u.northwestern.edu

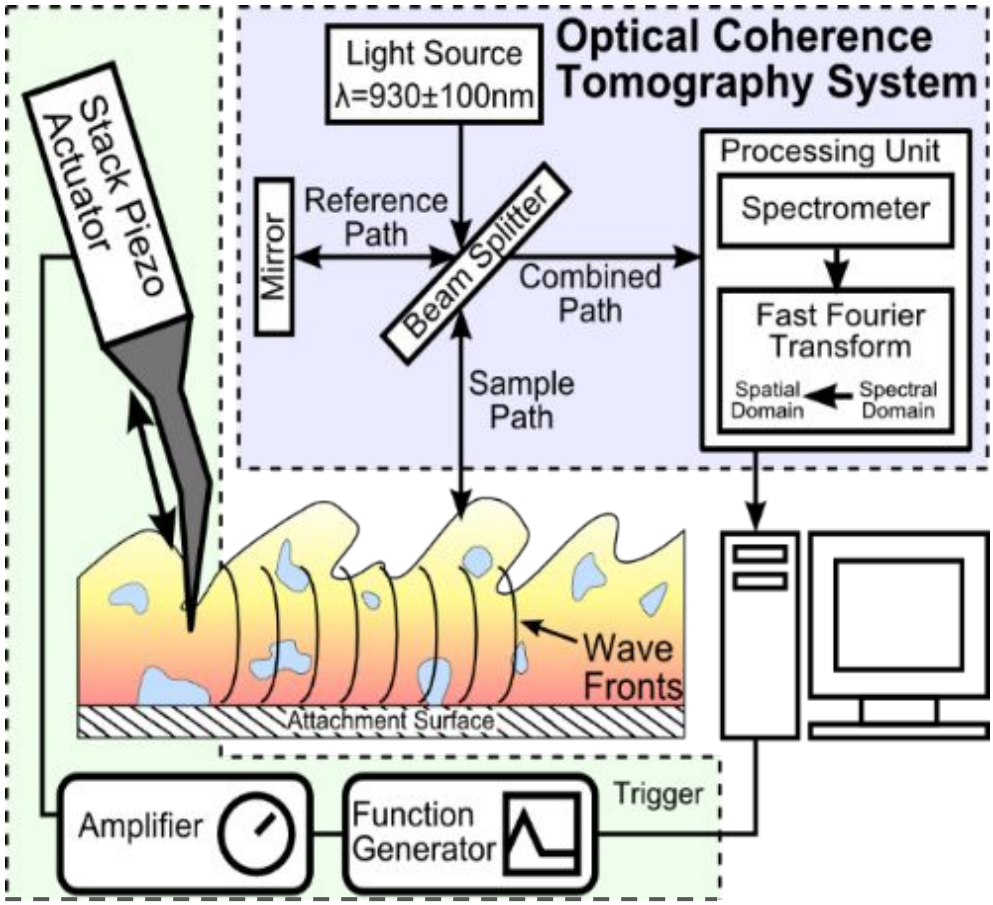

Fig. 1. Phase-sensitive optical coherence elastography setup

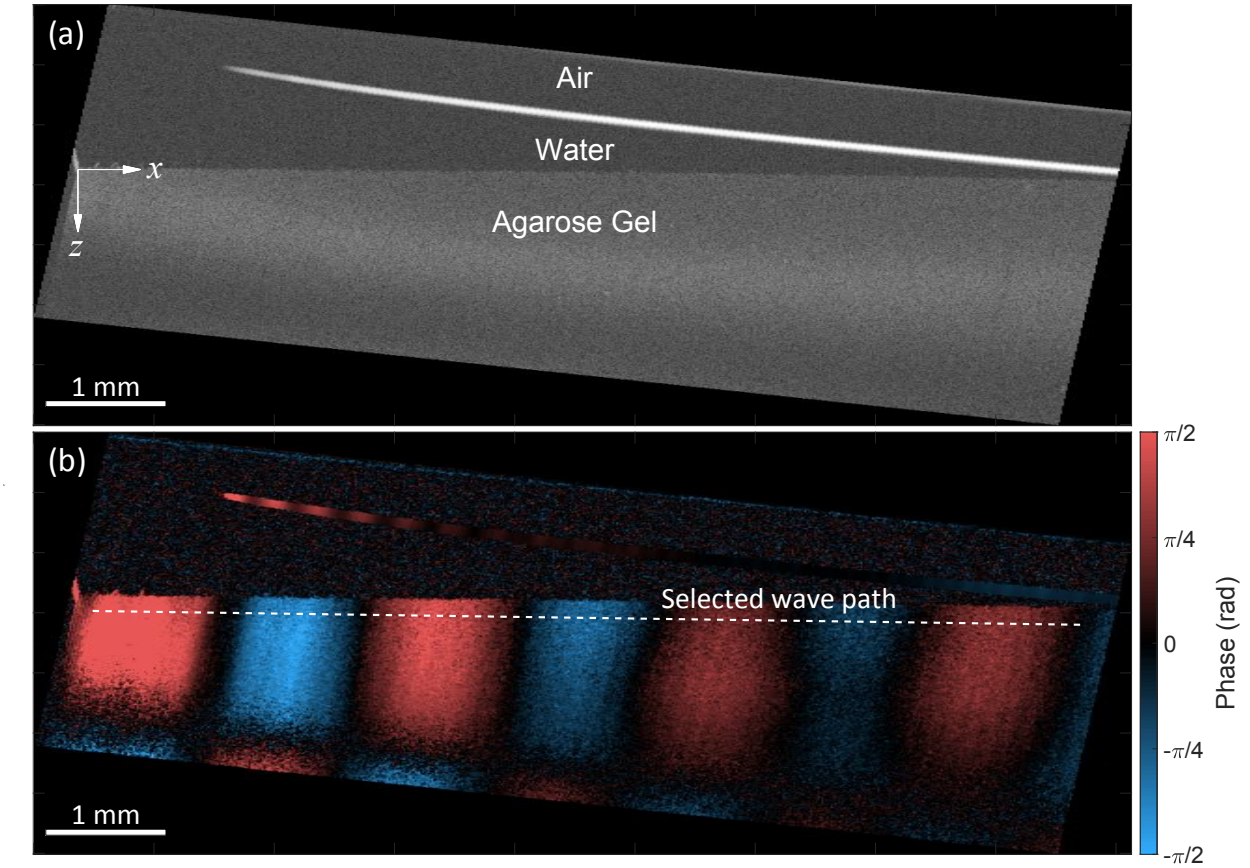

Fig. 2. (a) Optical coherence tomography image of a 2.0% agarose gel phantom. The thickness of the water layer was reduced in this figure for visualization purposes. The experiments were conducted with a water layer of >2 mm thickness. (b) Optical coherence elastography image showing phase distribution of 1.4 kHz elastic waves in the sample. The pixel sizes along the *x*- and *z*-directions are 4 and 2 μm.

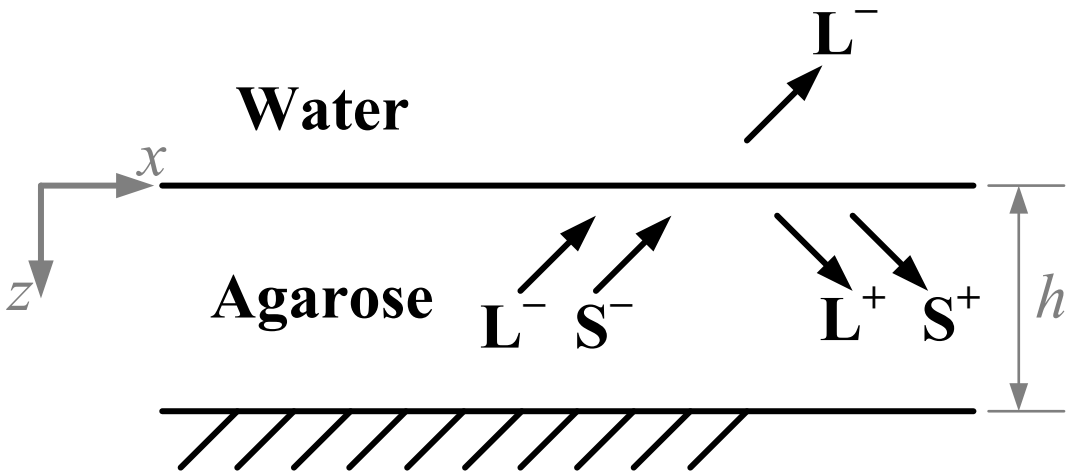

Fig. 3. Geometry of the layered numerical model. Symbols *L* and *S* represent compressional and shear waves. Positive and negative superscripts are used to represent forward and backward propagating partial waves.

(a)

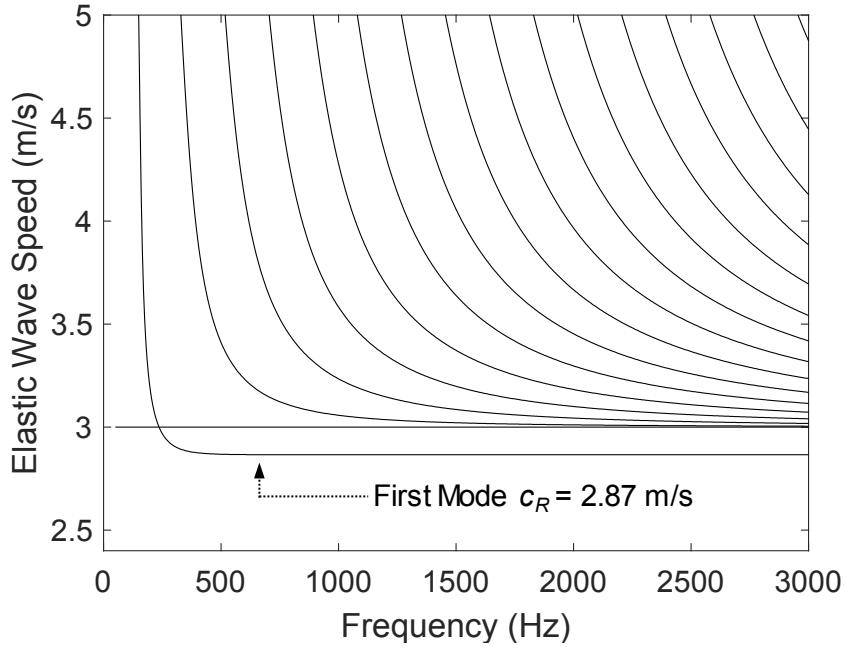
Elastic Wave Speed (m/s)
5
4.5
4
3.5
3
2.5
0
500
1000
1500
2000
2500
3000
Frequency (Hz)
First Mode c_R = 2.87 m/s

(b)

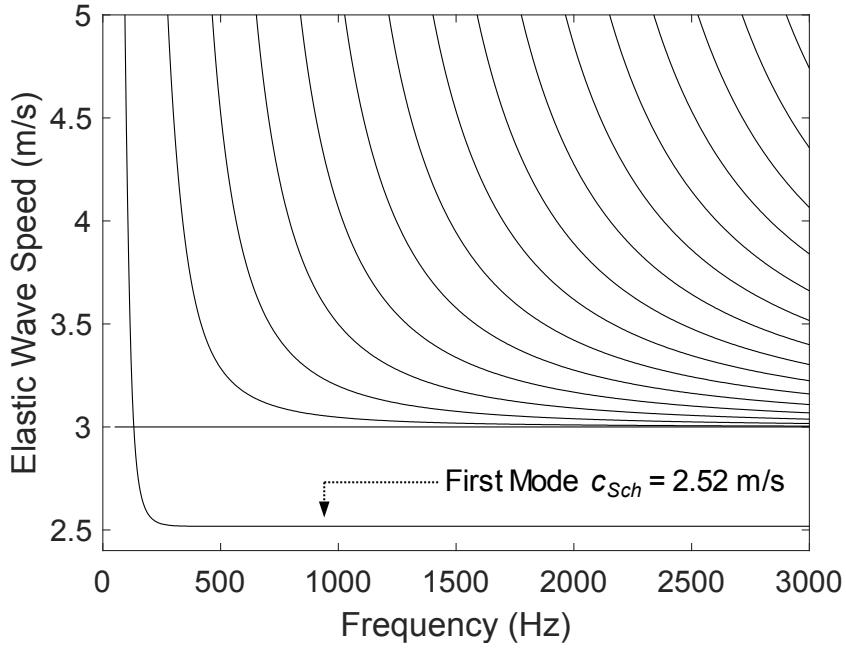
Elastic Wave Speed (m/s)
5
4.5
4
3.5
3
2.5
0
500
1000
1500
2000
2500
3000
Frequency (Hz)
First Mode c_{Sch} = 2.52 m/s

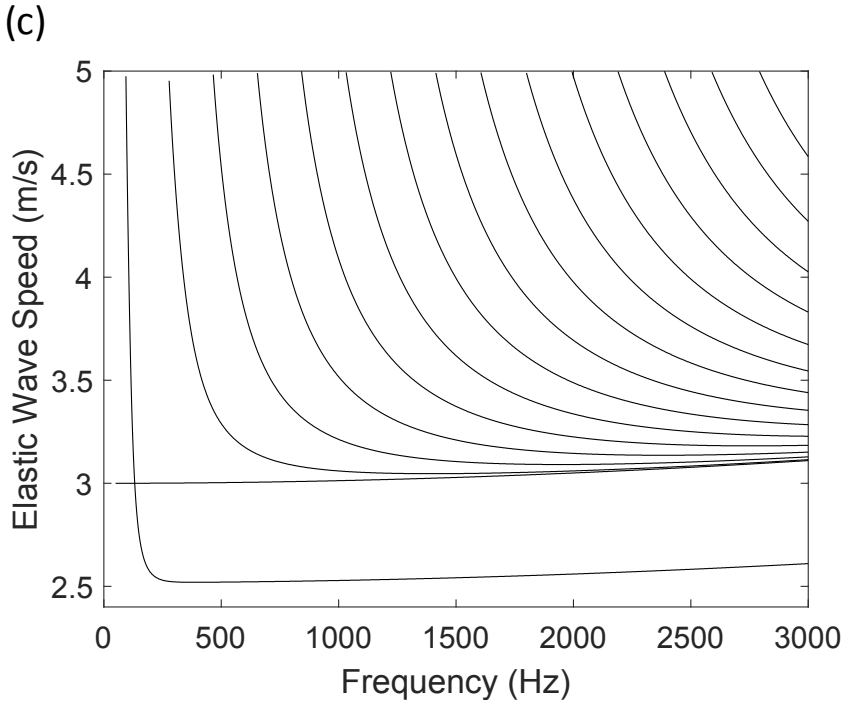

Fig. 4. Dispersion curves for (a) a pure-elastic layer with free-clamped boundary condition, (b) a pure-elastic plate with liquid loading on the top surface and clamped boundary condition at bottom surface, and (c) a viscoelastic layer with liquid loading and clamped boundary conditions. The layer thickness h =10 mm.

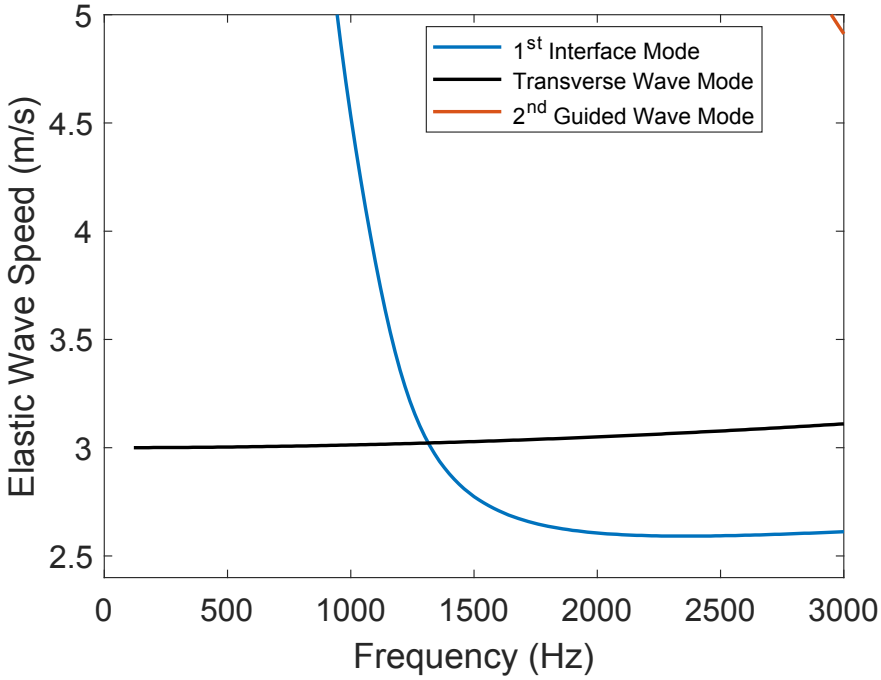

Fig. 5. Dispersion curves for a 1 mm thick viscoelastic layer with liquid loading and clamped boundary conditions.

(a)

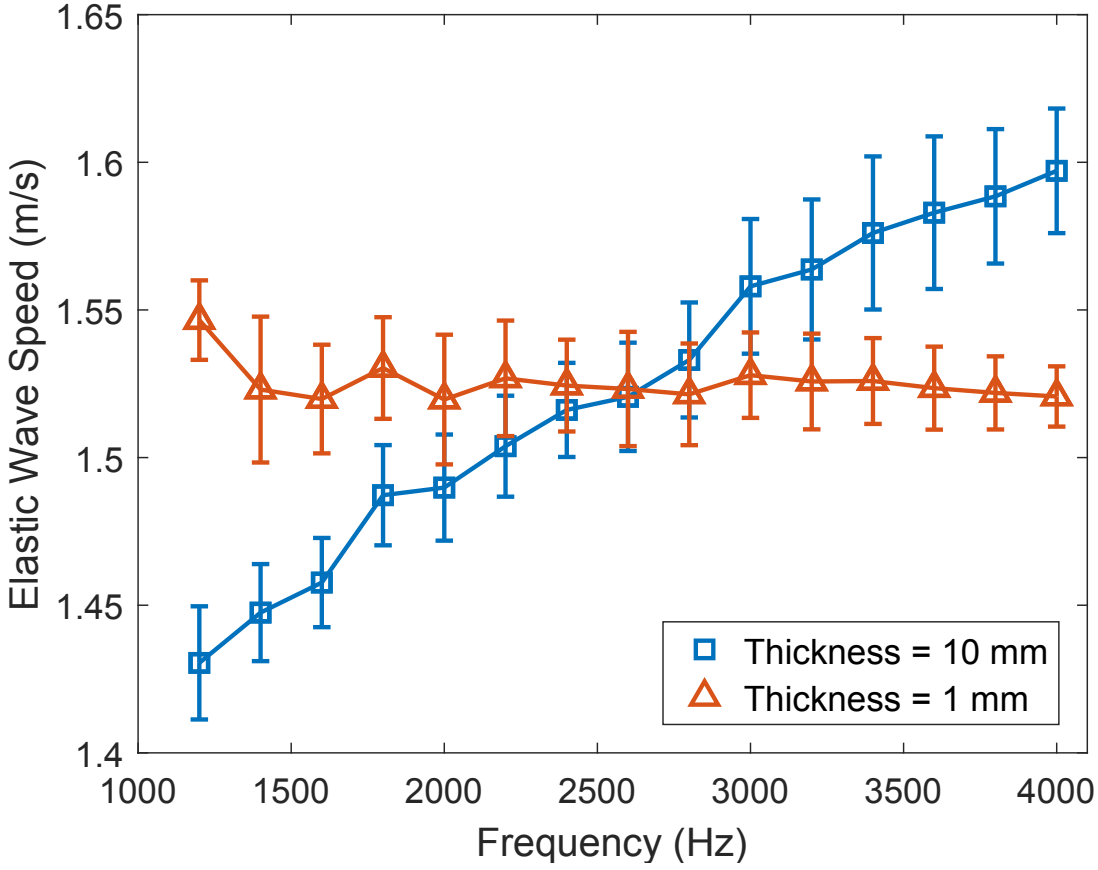
1.65
1.6
1.55
1.5
1.45
1.4
Elastic Wave Speed (m/s)
1000
1500
2000
2500
3000
3500
4000
Frequency (Hz)
Thickness = 10 mm
Thickness = 1 mm

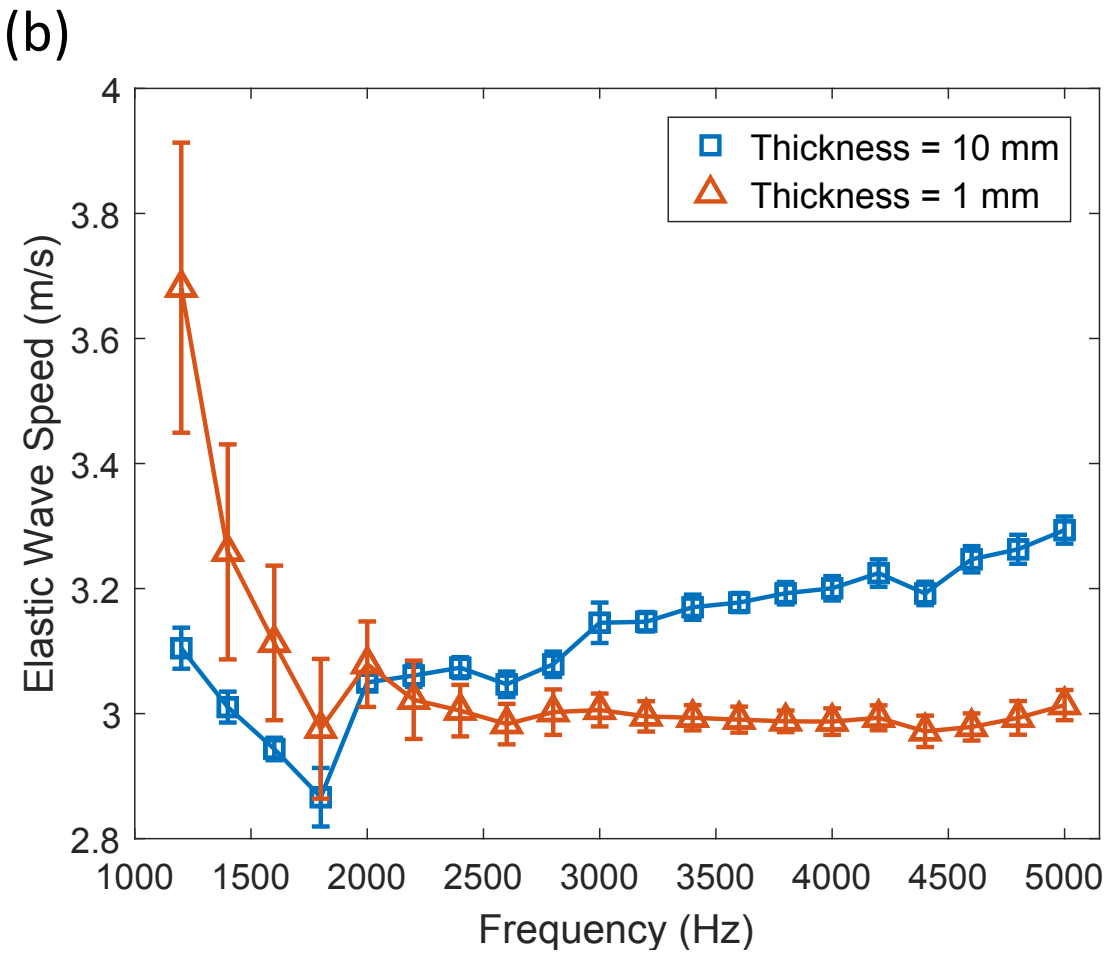

Fig. 6. Measured guided elastic wave dispersion curves in agarose gel phantoms with (a) 1.0% and (b) 2.0% agarose concentrations, for different sample thicknesses.

(a)

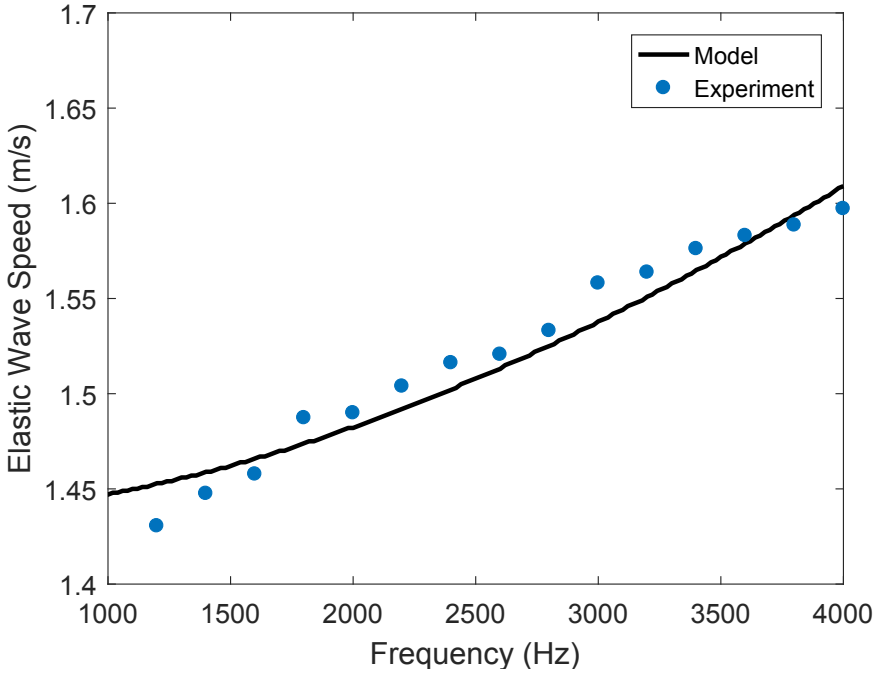
Model
Experiment
Elastic Wave Speed (m/s)
Frequency (Hz)
1.7
1.65
1.6
1.55
1.5
1.45
1.4
1000
1500
2000
2500
3000
3500
4000

(b)

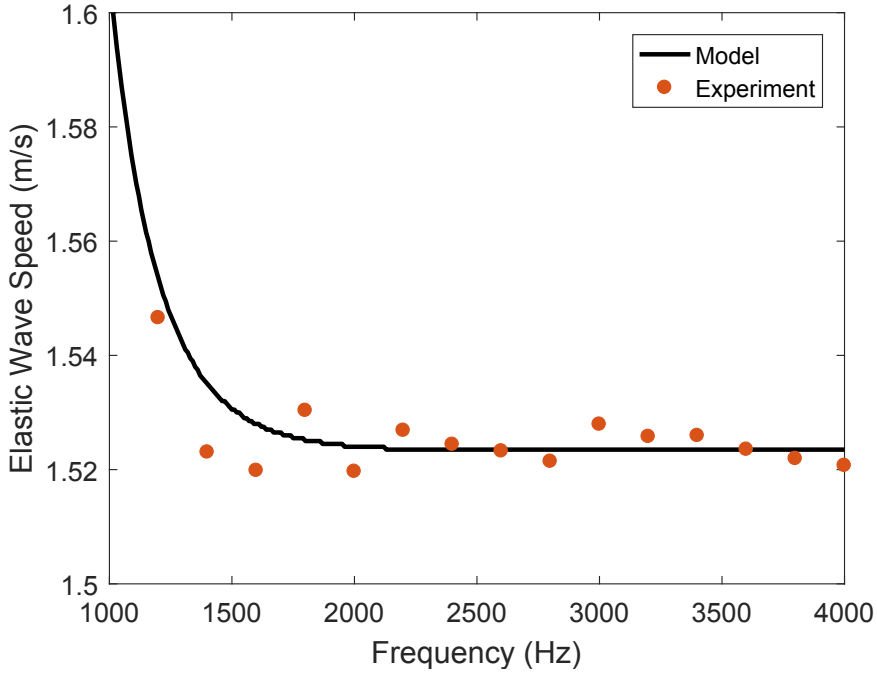
Model
Experiment
Elastic Wave Speed (m/s)
Frequency (Hz)
1.6
1.58
1.56
1.54
1.52
1.5
1000
1500
2000
2500
3000
3500
4000

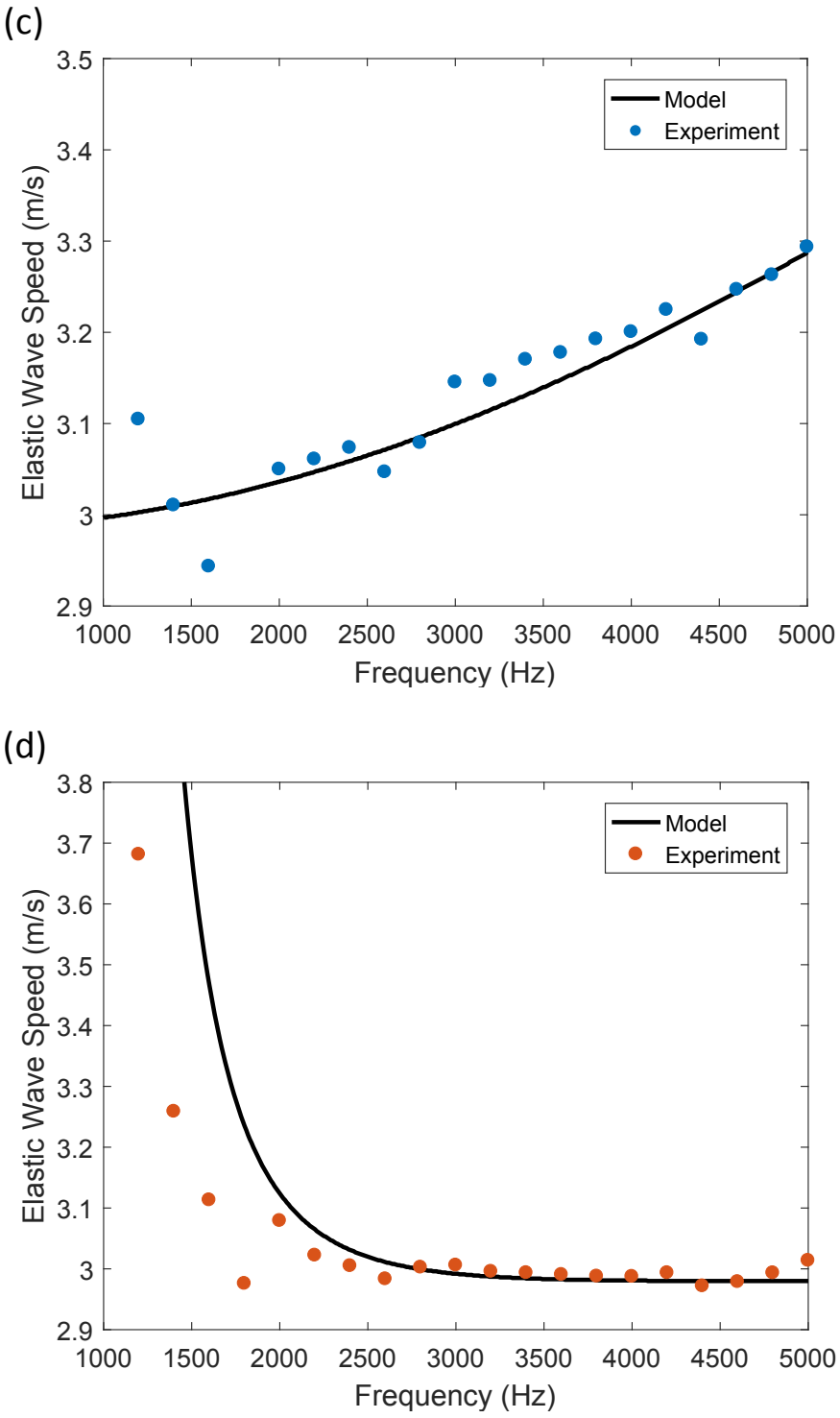

Fig. 7. Comparison of measured and numerical guided elastic wave dispersion curves in gel samples with 1.0% (a and b), and 2.0% (c and d) agarose concentrations, for different sample thicknesses. Sample thickness = 10 mm in (a) and (c), and 1 mm in (b) and (d). Model parameters are listed in Table 1.

Sample Properties	**(a)**	**(b)**	**(c)**	**(d)**
Agarose gel concentration	1.0%		2.0%	
Thickness (mm)	10	1	10	1
Shear Wave Speed (m/s)	1.71	1.81	3.55	3.55
Complex Shear Viscosity (Pa-s)	0.07		0.22	
Shear Modulus (kPa)	2.9	3.2	12.6	12.6

Table 1: Estimated mechanical properties for agarose gel phantoms by model

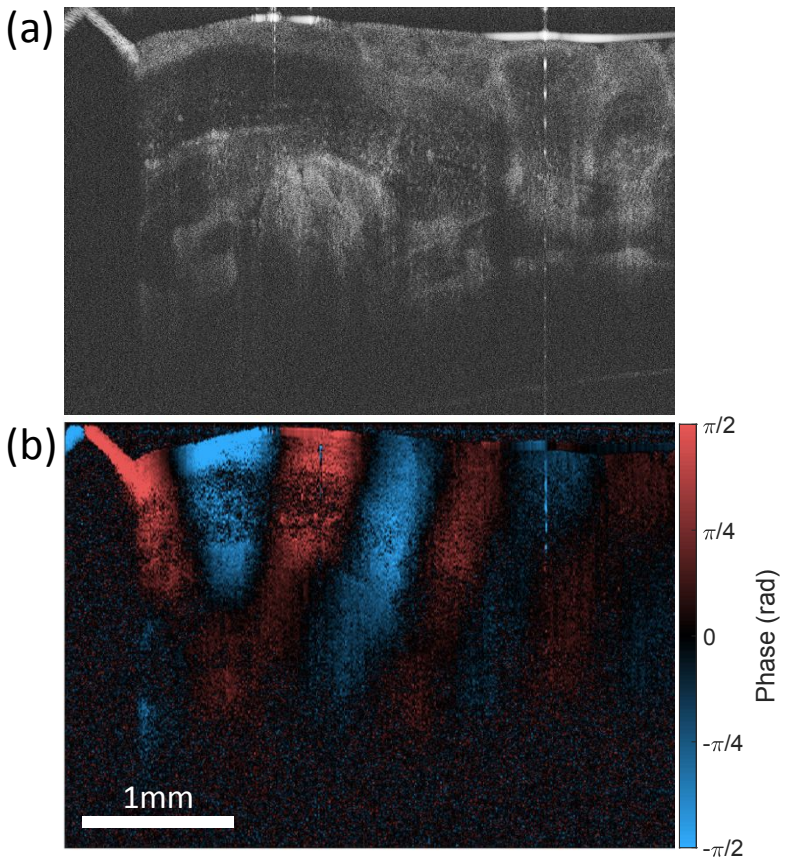
(a)
(b)
1mm
π/2
π/4
0
-π/4
-π/2
Phase (rad)

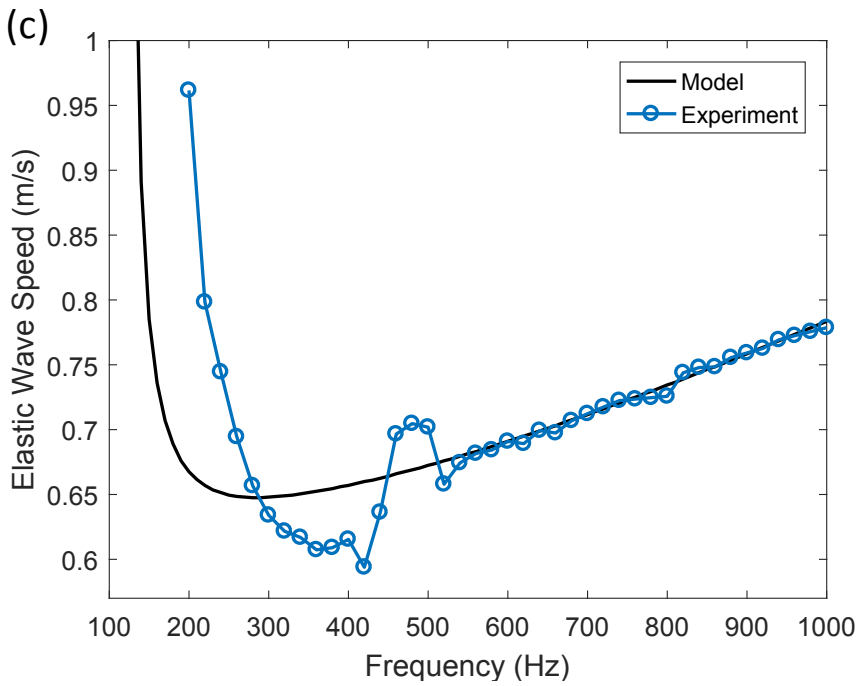
(c)
Model
Experiment
Elastic Wave Speed (m/s)
Frequency (Hz)
1
0.95
0.9
0.85
0.8
0.75
0.7
0.65
0.6
100
200
300
400
500
600
700
800
900
1000

Fig. 8. (a) Optical coherence tomography image of a mixed-culture bacterial biofilm, (b) optical coherence elastography image showing phase distribution of 660 Hz elastic waves in the sample, and (c) dispersion curves for the model (shear modulus 429 Pa and complex shear viscosity 0.06 Pa-s) and excited elastic waves in the sample.